Simulation of the Seasonal Variation of Mesospheric Zonal Wind Reversal with Anisotropic Gravity Waves

Tao Wang[1], Han-Li Liu[2], and Wenshou Tian[1]

[1]Lanzhou University
[2]National Center for Atmospheric Research, P. O. Box, 3000, Boulder, CO 80307-3000

March 6, 2023

Abstract

The observed seasonal variation of zonal wind reversal in the mesosphere and lower thermosphere (MLT) is often not well captured in whole atmosphere general circulation models (GCMs) with current gravity wave parameterization schemes. In this study, we investigate the possible physical mechanisms controlling this seasonal variation. It is found that adaptation of an anisotropic parameterized gravity wave source spectrum with stronger eastward and weaker westward propagating waves can reproduce this seasonal feature. Furthermore, additional stratospheric forcing is needed to control the large winter stratospheric zonal wind and alleviate the "cold-pole" problem in the southern winter. This is accomplished by the application of an inertial gravity wave parameterization scheme. With these changes, the Whole Atmosphere Community Climate Model with thermosphere and ionosphere extension (WACCM-X) can produce zonal mean zonal wind that is in better agreement with climatology from the stratosphere to MLT, including the seasonal variation of the zonal wind reversal.

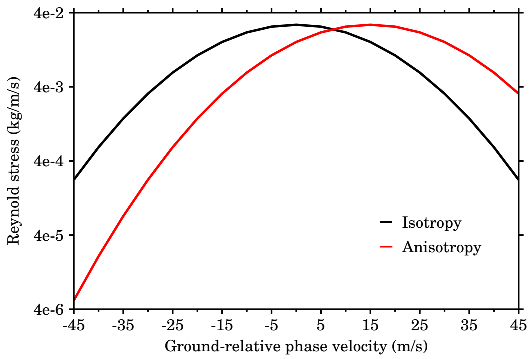

Reynold stress (kg/m/s)
4e-2
4e-3
4e-4
4e-5
4e-6
-45
-35
-25
-15
-5
5
15
25
35
45
Ground-relative phase velocity (m/s)
Isotropy
Anisotropy

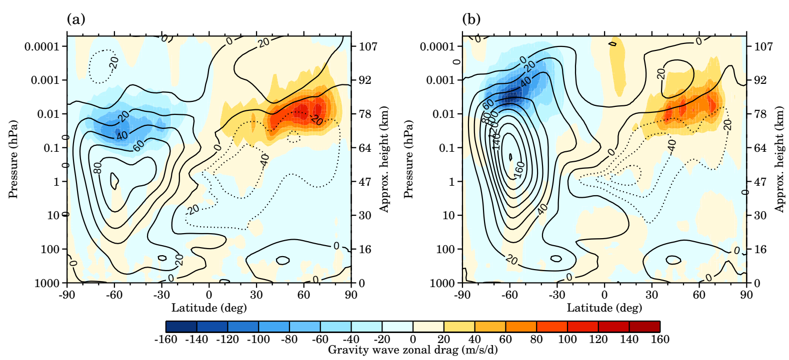

(a)
(b)
Pressure (hPa)
Approx. height (km)
Latitude (deg)
Gravity wave zonal drag (m/s/d)

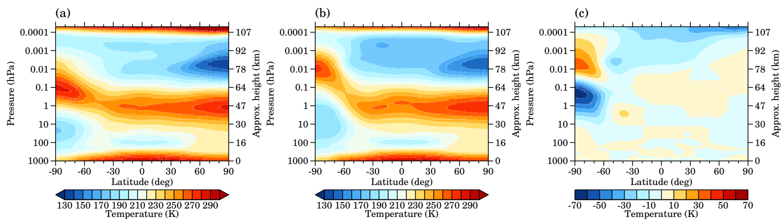
(a)
(b)
(c)
Pressure (hPa)
Approx. height (km)
Latitude (deg)
Temperature (K)

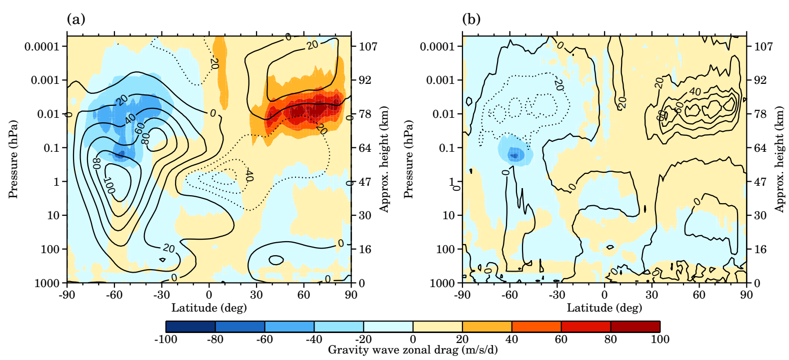
(a)
(b)
Pressure (hPa)
Approx. height (km)
Latitude (deg)
Gravity wave zonal drag (m/s/d)

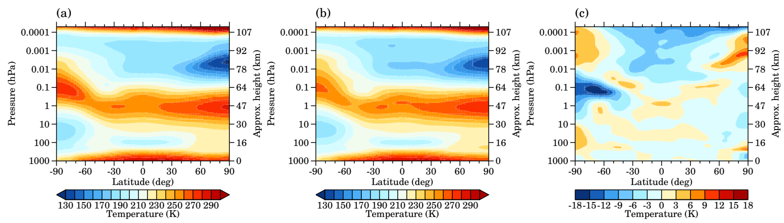
(a)
(b)
(c)
Pressure (hPa)
Approx. height (km)
Latitude (deg)
Temperature (K)

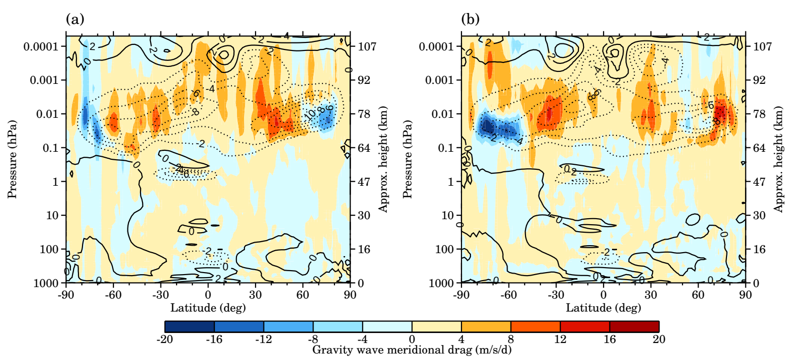
(a)
(b)
Pressure (hPa)
Approx. height (km)
Latitude (deg)
Gravity wave meridional drag (m/s/d)

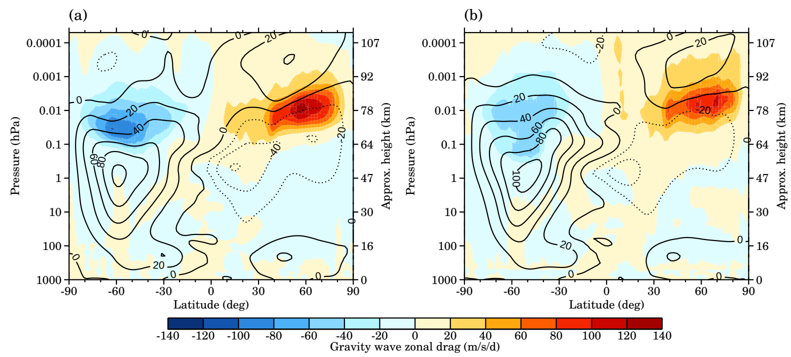
(a)
(b)
Pressure (hPa)
Approx. height (km)
Latitude (deg)
Gravity wave zonal drag (m/s/d)

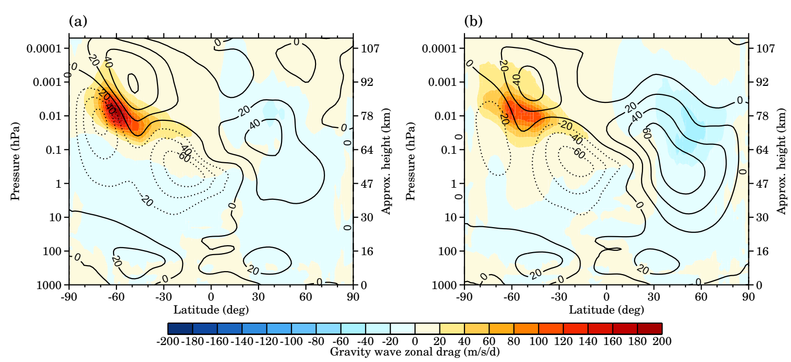
(a)
(b)
Pressure (hPa)
Approx. height (km)
Latitude (deg)
Gravity wave zonal drag (m/s/d)

Simulation of the Seasonal Variation of Mesospheric Zonal Wind Reversal with Anisotropic Gravity Waves

Tao Wang[1,2], Han-Li Liu[2], and Wenshou Tian[1]

[1]College of Atmospheric Sciences, Lanzhou University, Lanzhou, Gansu, China.

[2]High Altitude Observatory, National Center for Atmospheric Research, Boulder, CO, USA

*Corresponding author: Han-Li Liu (liuh@ucar.edu)

Key Points:

- The seasonal variation of zonal wind reversal is reproduced in the model by applying an anisotropic gravity wave parameterization scheme.
- An inertial gravity wave parameterization scheme is introduced in the model to alleviate the winter stratospheric jet and the cold-pole bias.
- The simulated wind structure in the stratosphere and mesosphere with the updated gravity wave parameterization scheme is more comparable to observations.

Abstract

The observed seasonal variation of zonal wind reversal in the mesosphere and lower thermosphere (MLT) is often not well captured in whole atmosphere general circulation models (GCMs) with current gravity wave parameterization schemes. In this study, we investigate the possible physical mechanisms controlling this seasonal variation. It is found that adaptation of an anisotropic parameterized gravity wave source spectrum with stronger eastward and weaker westward propagating waves can reproduce this seasonal feature. Furthermore, additional stratospheric forcing is needed to control the large winter stratospheric zonal wind and alleviate the "cold-pole" problem in the southern winter. This is accomplished by the application of an inertial gravity wave parameterization scheme. With these changes, the Whole Atmosphere Community Climate Model with thermosphere and ionosphere extension (WACCM-X) can produce zonal mean zonal wind that is in better agreement with climatology from the stratosphere to MLT, including the seasonal variation of the zonal wind reversal.

Plain Language Summary

Various radar and satellite observations have captured that the zonal wind reversal in the mesosphere and lower thermosphere has a seasonal variation with higher/weaker winter zonal wind reversal and lower/stronger summer zonal wind reversal. While this seasonal variation is generally not presented in the numerical model with current gravity wave parameterization schemes. We apply an anisotropic spectrum of parameterized gravity wave sources with stronger eastward and weaker westward propagating waves instead of the isotropic one to reproduce this seasonal variation in the numerical model. Furthermore, we introduce an inertial gravity wave parameterization scheme to reduce the large stratospheric jet in the southern winter. With the

updated gravity wave parameterization schemes, the simulated zonal wind structure is in better agreement with observations.

1 Introduction

The mesosphere-lower thermosphere (MLT) is a transition region coupling the Earth's atmosphere and the space environment, where both radiative and dynamical forcing play essential roles (e.g., Becker, 2012; Vincent, 2015). In particular, gravity wave (GW) breaking and dissipation is a key dynamical factor (e.g., Holton, 1982, 1983; Fritts and Alexander, 2003; Cai et al., 2017; Dong et al., 2021). The waves deposit momentum and energy to the background flow, drive mesospheric zonal wind reversals, and alter the summer-to-winter circulation in the MLT (e.g., Smith et al., 2011; Sato et al., 2012; Liu et al., 2023). These effects need to be parameterized in most general circulation models (GCMs) that include the middle and upper atmosphere, since they cannot be properly resolved in these models (e.g., McLandress, 1998; Garcia et al., 2007; Alexander et al., 2010; Ern et al., 2018; Medvedev and Yiğit, 2019).

While the parameterization schemes are essential for the GCMs to obtain the basic wind and temperature structures in the MLT, they are also a major source of model uncertainty and bias (Pedatella et al., 2014). One notable example of such bias is that the seasonal variation of the zonal wind reversal in the MLT is not well captured. As shown in Upper Atmosphere Research Satellite (UARS) measurements (McLandress et al., 1996, Figure 12; Swinbank and Ortland, 2003, Figure 5), the zonal mean zonal wind reverses from eastward to westward in the winter hemisphere at a higher altitude (between 0.001 and 0.0001 hPa, approximately 100 km), and from westward to eastward in the summer hemisphere at a lower altitude (between 0.01 and 0.001 hPa, approximately 85 km). The reversal strength also varies with seasons: weaker in the winter and stronger in the summer. This seasonal variation is also reported in ground-based wind observations (Stober et al., 2021; Hindley et al., 2022; Noble et al., 2022). While such seasonal variation is not properly captured in some of the GCMs, as indicated in the comparative analysis by Stober et al. (2021), Hindley et al. (2022), and Noble et al. (2022). For example, in WACCM-X as well as WACCM, the reversal levels are about the same in the winter and summer.

Possible causes for this seasonal variation have been suggested in previous studies. For GW parameterization schemes based on the linear saturation theory (Lindzen, 1981), the GW breaking level and strength are controlled by wave amplitude (and also wavelength). Based on this, Liu and Roble (2002) employed an anisotropic GW spectrum with its eastward wave sources stronger than the westward ones in the NCAR Thermosphere, Ionosphere, Mesosphere, and Electrodynamics General Circulation Model (TIME-GCM). The model was able to produce wind structures more comparable to the UARS observation in the MLT. Medvedev et al. (1998) and Yiğit et al. (2009) implemented a parameterized anisotropic/asymmetric GW spectrum to slow down the large stratospheric wind in the southern hemisphere. As shown in Yiğit et al. (2009), this scheme also leads to an intensified mesospheric eastward wind reversal in the northern hemisphere summer, though it does not seem to impact the height of the wind reversal. Becker and Vadas (2018) suggested that the eastward secondary GWs generated in the stratosphere and lower mesosphere (SLM) drive extra eastward zonal winds near the winter mesopause by comparing a high-resolution GW-resolving GCM against a coarse-resolution GW-parameterized GCM.

The zonal wind reversal height and strength are also closely associated with the primary zonal wind strength in the stratosphere and mesosphere. GWs, in addition to planetary waves, forcing can play an important role there. The so-called “cold-pole bias” is common to many GCMs, where the Antarctic winter is much colder compared to observations, and associated with it, the winter stratospheric jet is too strong and the breakdown of the polar vortex is too late (Hamilton et al., 1999, Austin et al., 2003). The cause of cold-pole bias in GCMs is suggested to be missing stratospheric GW forcing in the southern hemisphere winter (e.g., McLandress et al., 2012). Ern et al. (2018) presented enhanced GW activities at the southern mid-high latitude stratosphere in winter, where GCMs often produce insufficient GW forcing due to simplified GW parameterizations. Therefore, it is necessary to introduce such enhancement into GW parameterizations to improve the MLT circulation by slowing down the polar vortex and alleviating the cold pole bias (e.g., Yiğit et al., 2021). Garcia et al. (2017) applied a modified orographic GW parameterization with enhanced wave forcing in the southern winter stratosphere to reduce the cold-pole bias in WACCM. Other GW sources and scales, which may not be well accounted for in current parameterization schemes, can also play a role (Alexander et al., 2010; Xue et al., 2012; Liu, 2019; Vadas et al., 2018). For example, Xue et al. (2012) developed an inertial gravity wave (IGW) parameterization scheme to introduce additional stratospheric wave forcing to drive the quasi-biennial oscillation (QBO) in WACCM. The scheme is currently not included in the standard version of WACCM.

In this study, we investigate the effects of anisotropic GWs on the seasonal variation of the mesospheric zonal wind reversal using WACCM-X. We find it is also necessary to incorporate the IGW parameterization scheme into WACCM-X to control the winter stratospheric jet and reduce the cold-pole bias. In section 2, we provide a description of WACCM-X and the anisotropic GW and IGW parameterization schemes. In section 3, we present comparisons of simulation results applying the modified GW parameterization schemes with the current version. The conclusion and discussion are given in section 4.

2 Model and method

2.1 Whole Atmosphere Community Climate Model with thermosphere and ionosphere extension

WACCM-X is a self-consistent global model of the atmosphere extending from the earth's surface to the exobase. The current version of the model, WACCM-X v2.1, is used in this study. WACCM-X v2.1 is based on the NCAR Whole Atmosphere Community Climate Model 6 (WACCM6) physics package (Gettleman et al., 2019), with thermosphere and ionosphere physics and modifications to the dynamical core, as described in Liu et al. (2010, 2018). The version used has a horizontal resolution of 1.9° × 2.5° (latitude × longitude) and a vertical resolution of 0.25 scale heights above 1 hPa (higher and variable vertical resolution below), with 130 vertical levels from the earth's surface to 4.1×10^{-10} hPa (~500 to 700 km height). Free-running configuration (i.e., without any constraint by meteorological observations/reanalysis) is used in this study.

WACCM-X incorporates the same GW parameterization scheme as WACCM. Three types of GW sources, including orography (McFarlane, 1987), convection (Beres et al., 2005), and fronts (Richter et al., 2010), are parameterized in WACCM-X. Below the lower thermosphere, the effects of GWs are parameterized based on the linear saturation theory (Garcia et al., 2007, 2017). Above the MLT, we extend the GW parameterization schemes by considering the effects of molecular damping on GWs, which is to be discussed in a future paper.

2.2 Anisotropic gravity wave parameterization scheme

In the standard WACCM-X (WACCM-X v2.1), frontal GWs, which account for a large portion of the GW forcing at mid-high latitudes, are parameterized with an isotropic ground-based phase speed spectrum from -45 to 45 m/s and 2.5 m/s intervals. The spectral shape is a Gaussian distribution with its peak value at 0. In order to reproduce the seasonal variation of the wind reversal height and strength in the mesosphere, an anisotropic spectrum is used for the frontal GW source, by shifting the peak of the Gaussian distribution over phase speed from 0 to 15 m/s (eastward). Besides, to further enhance the anisotropy of the GW source spectrum, we change the Gaussian width from 30 to 20. Fig. 1 presents the concept map of the GW source spectrum as a function of ground-relative phase velocity. The black and red curves denote isotropic and anisotropic spectra of GW sources, respectively. This results in an overall weaker westward wave source and stronger eastward wave source (i.e., the GW source spectrum has a bias to the eastward flux). Based on the linear saturation theory (Lindzen, 1981), this will lead to a higher wave breaking altitude for the former and a lower wave breaking altitude for the latter.

2.3 Inertial gravity wave parameterization scheme

The IGW parameterization scheme applied is based on Xue et al. (2012), with the wave source tied to the frontal systems. The parameterized IGWs have an 800 km horizontal wavelength and a ground-based phase speed spectrum from -20 to 20 m/s with 2 m/s intervals. The spectral shape is a Gaussian distribution with its peak value at 0. It is noted that due to the numerical damping, only waves with horizontal wavelength larger than ~1500 km can be effectively resolved in FV WACCM-X with horizontal resolution of 1.9° × 2.5°. Thus, GWs with the 800 km horizontal wavelength cannot be well resolved in the model, and have to be parameterized.

2.4 Numerical experiments

In this study, we perform a 3-year simulation (after one year of spin-up) of free-running WACCM-X with the default GW parameterization scheme (hereafter the base case), 1-year simulation (after one year of spin-up) of free-running WACCM-X with the anisotropic GW source parameterization scheme (hereafter the control case 1), and 3-year simulation (after one year of spin-up) of free-running WACCM-X with the anisotropic GW source combined with IGW parameterization schemes (hereafter the control case 2). These cases are closely compared to examine the effects of the wave sources on the stratosphere and mesosphere. The base case and control case 2 are the focus of this study, and long simulations (3 model years) have been performed so the climatology is more rigorous.

3 Results

The zonal mean zonal GW drag and zonal wind in June simulated in the first year of the base case is presented in Fig. 2a. It is seen that the altitude and the magnitude of the westward GW drag are similar to those of the eastward GW drag in the MLT, with a -105 m/s/day peak between 0.1 and 0.01 hPa (~70 km) in the winter hemisphere and a 113 m/s/day peak around 0.01 hPa (~78 km) in the summer hemisphere. As a result, the mesospheric westward and eastward wind reversals are nearly symmetric between the two hemispheres/seasons, between 0.01 and 0.001 hPa (~80 km) at 60° in both hemispheres. The eastward wind reversal in Fig. 2a is comparable to the UARS climatology in the summer hemisphere. But the westward wind reversal in the UARS climatology in the winter hemisphere is between 0.001 and 0.0001 hPa (~100 km) at 60°S, which is approximately 20 km higher than that in Fig. 2a.

The simulation result in the control case 1 is shown in Fig. 2b. It is seen that due to the weaker westward GW sources, the altitude of mesospheric westward GW drag is overall higher, with the altitude of its peak value between 0.01 and 0.001 hPa (~85 km), driving a westward reversal around 0.001 hPa (~95 km) at 60°S. Meanwhile, the altitude of mesospheric eastward GW drag does not show a significant change, and consequently the altitude of mesospheric eastward wind reversal has little change. The result with regard to the altitude of the zonal wind reversal is thus more comparable with observations. However, the elevated mesospheric westward GW drag reduces the original westward GW forcing near the stratopause, resulting in an enhanced eastward jet near the stratopause. The maximum value of the eastward jet is up to 180 m/s in Fig. 2b, which is much stronger than that in Fig. 2a. The enhanced eastward jet not only impacts the upward propagating atmospheric waves but also leads to the cold-pole bias in the upper stratosphere.

Figures. 3a and 3b show the corresponding zonal mean temperature in June simulated in the first year of the base case and the control case 1, respectively. The difference between Figs. 3b and 3a is shown in Fig. 3c. It is seen that the winter stratosphere becomes colder (by up to 70 K) with the anisotropic GW wave source, which exacerbates the cold bias in that region. This also pushes the warm mesopause upward to ~0.001 hPa. Since the winter stratospheric temperature/wind bias is believed to be caused by insufficient wave forcing, the IGW parameterization is implemented to provide the stratospheric forcing.

Figure 4b presents the zonal mean zonal GW drag induced by the IGW (color shading) and by all other GW (line contours) in June simulated in the first year of the control case 2. The dissipation of IGW leads to a strong westward wave forcing peaking in SLM with a maximum value of -64 m/s/day. The westward wave forcing slows down the eastward jet in the southern hemisphere winter and consequently reduces the cold-pole bias by enhancing the downward branch of the Brewer-Dobson circulation and adiabatic warming. The eastward GW forcing due to IGW in the summer hemisphere is weak relative to the westward wave forcing, with a peak value of 9 m/s/day. The total zonal mean zonal GW drag, including IGW, is presented in Fig. 4a. The westward GW drag extends downward from MLT to the upper stratosphere due to the introduced IGW parameterization scheme. It is also noted that the westward forcing in the winter MLT in Fig. 4a is weaker and lower than that in Fig. 2b. This results from the slower background wind in SLM with the IGW forcing and thus reduces the intrinsic phase speed of upward propagating GWs. According to the linear saturation theory, the forcing by breaking GWs is proportional to the cube of the intrinsic phase speed. Overall, the pattern/strength of westward wave forcing is more dispersive/weaker relative to that of eastward wave forcing in the MLT, and the vertical gradient of westward wave forcing is also weaker against to that of eastward wave forcing in the MLT.

The zonal mean temperature in June simulated in the first year of the base case and the control case 2 are presented in Figs. 5a and 5b, respectively. The difference between Figs. 5b and 5a is shown in Fig. 5c. As mentioned above, owing to the additional westward forcing from IGW, the stratospheric eastward jet decreases and the downward branch of the Brewer-Dobson circulation strengthens. Consequently, the Antarctic stratosphere becomes warmer (by up to 6 K) in Fig. 5b relative to that in Fig. 5a, thus alleviating the cold bias by the anisotropic GW parameterization scheme only. Moreover, the location and temperature of the warm area in the Antarctic mesosphere in Fig. 5b are more similar to those in Fig. 5a. Overall, these temperature discrepancies in the Antarctic stratosphere and mesosphere resulted from the anisotropic GW parameterization scheme are apparently decreased by introducing the IGW parameterization scheme.

In contrast to the zonal wave forcing, the zonal mean meridional wave forcing and meridional wind in June simulated in the first year of the base case and control case 2 are presented in Figs. 6a and 6b, respectively. It is seen that the magnitude of the zonal mean meridional wave forcing and meridional wind is relatively small compared to those of zonal mean zonal wave forcing and wind in the MLT. Besides, the zonal mean meridional wave forcing and wind do not have a large discrepancy between the two. In the GW parameterization scheme used by WACCM-X (and also in WACCM), the GW spectrum is specified along the direction of the horizontal wind at the launch level. This approach is cost effective than specifying zonal and meridional wave sources separately, but it may also create an artificial coupling of the zonal and meridional wave sources. In this study, we focus on the zonal wave forcing and its effects on the background field in this study. Examination of the meridional GW parameterization scheme will be extended in future work.

In order to verify the robustness of the model results, the model climatology is obtained from the 3-year average. The 3-year averaged zonal mean zonal GW drag and zonal wind in the base case and control case 2 are presented in Fig. 7a and 7b, respectively. The most notable change is that the reversal level in the winter hemisphere at the middle and high latitude increases from right above 0.01 hPa (~80 km) in the base case to around 0.001 hPa (~90 km) in the control case 2. By contrast, the altitude of the wind reversal in the summer hemisphere (between 0.01 and 0.001 hPa) does not show a significant change.

The eastward jet in the control case 2 is robustly weakened due to IGW forcing (~110 m/s maximum), which is comparable to that in the base case (~105 m/s maximum). The maximum wind speed in the control case 2 decreases by ~70 m/s relative to that in the control case 1 (Fig. 2b). The westward jet in the control case 2, with a -55 m/s maximum wind speed, is slightly weaker than that in the base case, with a -61 m/s maximum wind speed, likely due to the weakened eastward wave forcing in the SLM introduced by IGW parameterization. Overall, the seasonal variation of mesospheric zonal wind reversals in June is reasonably well reproduced in the control case 2, and zonal mean zonal winds in the SLM have barely changed.

Figure 8 is the same as Figure 7, but for December. Unlike in June, the intensity of mesospheric eastward GW drag is much stronger than that of mesospheric westward GW drag in December in both the base case and control case 2. The altitude of mesospheric eastward GW drag in the base case is close to that in the control case 2, driving a nearly identical mesospheric eastward zonal wind reversal (between 0.1 and 0.01 hPa, ~70 km at 60°S) in both cases. More quantitively, the strength of mesospheric eastward GW drag in the control case 2 is weaker than that in the base case, with a 127 m/s/day maximum wave forcing in the control case 2 compared to 193 m/s/day maximum wave forcing in the base case. As a result, the mesospheric eastward wind reversal in the control case 2 is reduced by ~20 m/s relative to that in the base case, which is more comparable with observations. Note that Stober et al. (2021, Figure 2) reveals that the maximum strength of mesospheric eastward wind reversal in the southern winter at mid-high latitudes represented by WACCM-X with isotropic GW parameterization scheme is above 40 m/s, which is much higher than that in long-term Davis meteor radar station (around 20 m/s). Similar results are also presented in Hindley et al. (2022, Figure 8) and Noble et al. (2022, Figure 3). On the other hand, the mesospheric westward GW drag in the base case is rather weak, with a -30 m/s/day maximum wave forcing, driving a westward zonal wind reversal that is weak (not too much below 0). In the control case 2, the westward wind reversal remains weak, with the reversal level between 0.01 and 0.001 hPa (~85 km). This is somewhat lower than the 0.001 hPa reversal level from UARS climatology, but still generally higher than the eastward reversal level in the southern summer hemisphere.

It is worth noting that UARS exhibits a stronger eastward jet relative to a weaker westward jet in SLM in all seasons (except in January when the two are more comparable, Swinbank and Ortland, 2002, Figure 5), suggesting a weaker westward wave forcing compared to a stronger eastward wave forcing in SLM. This feature is also reproduced in June and December in the control case 2 due to the modified weaker westward GW sources and stronger eastward GW sources, but not for December in the base case. The strength of the eastward jet is weaker than that of the westward jet in December in the base case, which is opposite to that in UARS and the control case 2.

4 Conclusion and discussion

In this paper, we investigate the possible physical mechanisms controlling the seasonal variation of mesospheric zonal wind reversals, including the reversal altitude and strength. We found it is necessary to adapt an anisotropic GW spectrum, which mainly impacts the MLT, and apply an IGW parameterization scheme, which mainly impacts the SLM, in the WACCM-X. In the base case, WACCM-X with the isotropic GW source parameterization scheme produces seasonally/hemispherically symmetric mesospheric zonal wind reversals, which differs from observations. In the control case 1, by incorporating an anisotropic GW spectrum with stronger eastward and weaker westward waves in the GW parameterization scheme, WACCM-X can qualitatively reproduce the seasonal variational of mesospheric zonal wind reversals, but it induces an excessively strong stratospheric eastward wind jet and large cold-pole bias in the southern winter due to weaker westward frontal GWs. This is ameliorated by applying the IGW parameterization scheme. While anisotropic/asymmetric GW spectrum has been applied in previous studies (Medvedev et al., 1998; Yiğit et al., 2008, 2009), the wave effects differ in that therein (i) the anisotropic spectrum shifted eastward carries a more negative (westward) flux and acts to slow down the stratospheric jet, and (ii) the parameterization affects the strength but not the height of the zonal wind reversal in the MLT.

Further study reveals that in the control case 2, WACCM-X with combined anisotropic GW and IGW parameterization schemes apparently reduces the stratospheric eastward wind jet and large cold-pole bias in the southern winter and reproduces the overall seasonal variation of mesospheric zonal wind reversals. The anisotropy of GWs with stronger eastward and weaker westward components is also consistent with the analysis of GW spectra obtained in high-resolution WACCM-X simulations (Liu et al., 2023). The study suggests that the anisotropic GWs and large scale GWs play important roles in the middle and upper atmosphere momentum budget. The mesospheric eastward jet in the southern hemisphere summer has little change compared to the isotropic GW parameterization scheme. The weak mesospheric westward zonal wind reversal as well as the too strong eastward mesospheric wind reversal in December is improved in the control case 2. In addition, the wind climatology in the SLM, with the eastward jet being stronger than that of the westward jet, is better resolved in the control case 2. Overall, the simulated wind structure from the stratosphere and lower thermosphere with updated GW parameterization schemes is more comparable to observations.

In addition, the meridional propagation of the GWs, especially the poleward propagation along the easterly jet in the summer hemisphere (e.g., Sato et al., 2009; Preusse et al., 2009; Chen et al., 2019; Thurairajah et al., 2020; Forbes et al., 2022) can have important implications for wave forcing and wind reversal in the MLT region. However, the horizontal propagation of

GW is not taken into consideration in current schemes. In the current parameterization, the strong eastward forcing at middle and high latitudes in the summer MLT comes mostly from parameterized forcing from frontogenesis and convection. This could be a large discrepancy in comparison to the actual forcing by waves coming from lower latitudes and lower altitudes. This could be responsible for the difference between the simulated and observed wind reversal in the summer mesopause region, with the simulated wind reversal much weaker than the UARS climatology at middle and high latitudes. It is also interesting to note that this wind feature is better resolved in high-resolution WACCM-X simulations, where the wind reversal is driven by resolved GWs (Liu et al., 2023).

Acknowledgments

We thank R. R. Garcia, A. K. Smith and B. Tan for their extension of the inertial gravity wave parameterization scheme. We thank N. Pedatella for his helpful comments on our manustript and J. McInerney for his guidance about WACCM-X operation. This work is partly supported by the National Natural Science Foundation of China (42130601, 42142038). Tao Wang is partly supported by a fellowship from China Scholarship Council (CSC No. 201906180060) and the HAO Visitor Program. This material is based on work supported by the National Center for Atmospheric Research (NCAR), which is a major facility sponsored by the NSF under Cooperative Agreement 1852977.

Data Availability Statement

The simulation is based on Whole Atmosphere Community Climate Model with thermosphere and ionosphere extension (WACCM-X) version 2.1.3, which is part of NCAR Community Earth System Model (CESM) version 2.1.3. It is available for download at https://github.com/ESCOMP/CESM/releases/tag/release-cesm2.1.3/. The simulation output used to generate this study's figures will be placed in a Zenodo repository prior to publication.

References

Austin, J., Shindell, D., Beagley, S. R., Brühl, C., Dameris, M., Manzini, E., ... & Shepherd, T. G. (2003). Uncertainties and assessments of chemistry-climate models of the stratosphere. *Atmospheric Chemistry and Physics*, 3(1), 1-27. https://doi.org/10.5194/acp-3-1-2003, 2003.

Alexander, M. J., Geller, M., McLandress, C., Polavarapu, S., Preusse, P., Sassi, F., et al. (2010). Recent developments in gravity-wave effects in climate models and the global distribution of gravity-wave momentum flux from observations and models. *Quarterly Journal of the Royal Meteorological Society*, 136, 1103–1124. https://doi.org/10.1002/qj.637

Beres, J. H., Garcia, R. R., Boville, B. A., & Sassi, F. (2005). Implementation of a gravity wave source spectrum parameterization dependent on the properties of convection in the Whole Atmosphere Community Climate Model (WACCM). *Journal of Geophysical Research: Atmospheres*, 110(D10). doi:10.1029/2004JD005504.

Becker, E. (2012). Dynamical control of the middle atmosphere. *Space Science Reviews*, 168(1), 283-314. doi: 10.1007/s11214-011-9841-5.

Becker, E., & Vadas, S. L. (2018). Secondary gravity waves in the winter mesosphere: Results from a high-resolution global circulation model. *Journal of Geophysical Reseach: Atmospheres*, 123, 2605–2627. https://doi.org/10.1002/2017JD027460.

Cai, X., Yuan, T., & Liu, H. L. (2017). Large-scale gravity wave perturbations in the mesopause region above Northern Hemisphere midlatitudes during autumnal equinox: A joint study by the USU Na lidar and Whole Atmosphere Community Climate Model. *Annales Geophysicae*, 35, 181–188. https://doi.org/10.5194/angeo-35-181-2017.

Chen, D., Strube, C., Ern, M., Preusse, P., & Riese, M. (2019). Global analysis for periodic variations in gravity wave squared amplitudes and momentum fluxes in the middle atmosphere. Ann. Geophys., 37, 487-506, https://doi.org/10.5194/angeo-37-487-2019.

Dong, W., Hickey, M. P., & Zhang, S. (2021). A Numerical Study of Gravity Waves Propagation Characteristics in the Mesospheric Doppler Duct. *Journal of Geophysical Research: Atmospheres*, 126(13), e2021JD034680. https://doi.org/10.1029/2021JD034680.

Ern, M., Trinh, Q. T., Preusse, P., Gille, J. C., Mlynczak, M. G., Russell III, J. M., 705 & Riese, M. (2018). Gracile: a comprehensive climatology of atmospheric gravity wave parameters based on satellite limb soundings. *Earth System Science Data*, 10 , 857-892. doi: 10.5194/essd-10-857-2018.

Fritts, D. C., & Alexander, M. J. (2003). Gravity wave dynamics and effects in the middle atmosphere. *Reviews of geophysics*, 41(1). https://doi.org/10.1029/2001RG000106.

Forbes, J. M., Ern, M., & Zhang, X. (2022). The global monsoon convective system as reflected in upper atmosphere gravity waves. Journal of Geophysical Research: Space Physics, 127, e2022JA030572, https://doi.org/10.1029/2022JA030572.

Garcia, R. R., Marsh, D. R., Kinnison, D. E., Boville, B. A., & Sassi, F. (2007). Simulation of secular trends in the middle atmosphere, 1950–2003. *Journal of Geophysical Research: Atmospheres*, 112(D9), doi:10.1029/2006JD007485.

Garcia, R. R., Smith, A. K., Kinnison, D. E., de la Cámara, Á., & Murphy, D. J. (2017). Modification of the gravity wave parameterization in the Whole Atmosphere Community Climate Model: Motivation and results. *Journal of the Atmospheric Sciences*, 74(1), 275-291, doi: 10.1175/JAS-D-16-0104.1.

Gettelman, A., Mills, M. J., Kinnison, D. E., Garcia, R. R., Smith, A. K., Marsh, D. R., ... & Randel, W. J. (2019). The whole atmosphere community climate model version 6 (WACCM6). *Journal of Geophysical Research: Atmospheres*, 124(23), 12380-12403. https://doi.org/10.1029/2019JD030943.

Holton, J. R. (1982). The role of gravity wave induced drag and diffusion in the momentum budget of the mesosphere. *Journal of Atmospheric Sciences*, 39(4), 791-799. https://doi.org/10.1175/1520-0469(1982)039<0791:TROGWI>2.0.CO;2.

Holton, J. R. (1983). The influence of gravity wave breaking on the general circulation of the middle atmosphere. *Journal of Atmospheric Sciences*, 40(10), 2497-2507. https://doi.org/10.1175/1520-0469(1983)040<2497:TIOGWB>2.0.CO;2.

Hamilton, K., Wilson, R. J., & Hemler, R. S. (1999). Middle atmosphere simulated with high vertical and horizontal resolution versions of a GCM: Improvements in the cold pole bias and generation of a QBO-like oscillation in the tropics. *Journal of the atmospheric sciences*, 56(22), 3829-3846. https://doi.org/10.1175/1520-0469(1999)056<3829:MASWHV>2.0.CO;2.

Hindley, N. P., Mitchell, N. J., Cobbett, N., Smith, A. K., Fritts, D. C., Janches, D., ... & Moffat-Griffin, T. (2022). Radar observations of winds, waves and tides in the mesosphere and lower thermosphere over South Georgia island (54° S, 36° W) and comparison with WACCM simulations. Atmospheric Chemistry and Physics, 22(14), 9435-9459. https://doi.org/10.5194/acp-22-9435-2022.

Lindzen, R. S. (1981), Turbulence and stress due to gravity wave and tidal breakdown, *Journal of Geophysical Research*, 86, 9701– 9714.

Liu, H. L., & Roble, R. G. (2002). A study of a self-generated stratospheric sudden warming and its mesospheric–lower thermospheric impacts using the coupled TIME-GCM/CCM3. *Journal of Geophysical Research: Atmospheres*, 107(D23), 4695, doi:10.1029/2001JD001533.

Liu, H. L., Foster, B. T., Hagan, M. E., McInerney, J. M., Maute, A., Qian, L., ... & Oberheide, J. (2010). Thermosphere extension of the whole atmosphere community climate model. *Journal of Geophysical Research: Space Physics*, 115(A12), doi:10.1029/2010JA015586.

Liu, H. L., Bardeen, C. G., Foster, B. T., Lauritzen, P., Liu, J., Lu, G., ... & Wang, W. (2018). Development and validation of the Whole Atmosphere Community Climate Model with thermosphere and ionosphere extension (WACCM-X 2.0). *Journal of Advances in Modeling Earth Systems*, 10(2), 381-402, doi: 10.1002/2017MS001232.

Liu, X., Xu, J., Yue, J., Vadas, S. L., & Becker, E. (2019). Orographic primary and secondary gravity waves in the middle atmosphere from 16-year SABER observations. Geophysical Research Letters, 46(8), 4512-4522.

Liu, H. L., Peter Hjort Lauritzen, Francis Vitt, & Steve Goldhaber (2023). Thermospheric and Ionospheric Effects by Gravity Waves from the Lower Atmosphere. *Journal of Geophysical Research - Space Physics*, doi: 10.1002/essoar.10511744.1.

McFarlane, N. A. (1987). The effect of orographically excited gravity wave drag on the general circulation of the lower stratosphere and troposphere. *Journal of Atmospheric Sciences*, 44(14), 1775-1800, doi: 10.1175/1520-0469(1987)044<1775:TEOOEG>2.0.CO;2.

McLandress, C., Shepherd, G. G., & Solheim, B. H. (1996). Satellite observations of thermospheric tides: Results from the Wind Imaging Interferometer on UARS. *Journal of Geophysical Research: Atmospheres*, 101(D2), 4093-4114. https://doi.org/10.1029/95JD03359.

McLandress, C. (1998). On the importance of gravity waves in the middle atmosphere and their parameterization in general circulation models. *Journal of Atmospheric and Solar-Terrestrial Physics*, 60(14), 1357-1383. https://doi.org/10.1016/S1364-6826(98)00061-3.

McLandress, C., Shepherd, T. G., Polavarapu, S., & Beagley, S. R. (2012). Is missing orographic gravity wave drag near 60° S the cause of the stratospheric zonal wind biases in chemistry–climate models?. Journal of the Atmospheric Sciences, 69(3), 802-818. https://doi.org/10.1175/JAS-D-11-0159.1

Medvedev, A. S., Klaassen, G. P., & Beagley, S. R. (1998). On the role of an anisotropic gravity wave spectrum in maintaining the circulation of the middle atmosphere. Geophysical research letters, 25(4), 509-512. https://doi.org/10.1029/98GL50177.

Medvedev, A. S., & Yiğit, E. (2019). Gravity waves in planetary atmospheres: Their effects and parameterization in global circulation models. *Atmosphere*, 10(9), 531. https://doi.org/10.3390/atmos10090531.

Noble, P., Hindley, N., Wright, C., Cullens, C., England, S., Pedatella, N., ... & Moffat-Griffin, T. (2022). Interannual variability of winds in the Antarctic mesosphere and lower thermosphere over Rothera (67 S, 68 W) in radar observations and WACCM-X. Atmospheric Chemistry and Physics Discussions, 1-29. https://doi.org/10.5194/acp-2022-150, 2022.

Pedatella, N. M., Fuller-Rowell, T., Wang, H., Jin, H., Miyoshi, Y., Fujiwara, H., ... & Goncharenko, L. (2014). The neutral dynamics during the 2009 sudden stratosphere warming simulated by different whole atmosphere models. *Journal of Geophysical Research: Space Physics*, 119(2), 1306-1324. https://doi.org/10.1002/2013JA019421.

Preusse, P., Eckermann, S. D., Ern, M., Oberheide, J., Picard, R. H., Roble, R. G., Riese, M., Russell III, J. M., & Mlynczak, M. G. (2009). Global ray tracing simulations of the SABER gravity wave climatology. J. Geophys. Res., 114, D08126, https://doi.org/10.1029/2008JD011214.

Richter, J. H., Sassi, F., & Garcia, R. R. (2010). Toward a physically based gravity wave source parameterization in a general circulation model. *Journal of the Atmospheric Sciences*, 67(1), 136-156, doi: 10.1175/2009JAS3112.1.

Swinbank, R., & Ortland, D. A. (2003). Compilation of wind data for the Upper Atmosphere Research Satellite (UARS) reference atmosphere project. *Journal of Geophysical Research: Atmospheres*, 108(D19), 4615. doi:10.1029/2002JD003135.

Smith, A. K., Garcia, R. R., Marsh, D. R., & Richter, J. H. (2011). WACCM simulations of the mean circulation and trace species transport in the winter mesosphere. *Journal of Geophysical Research: Atmospheres*, 116(D20). https://doi.org/10.1029/2011JD016083.

Sato, K., Watanabe, S., Kawatani, Y., Tomikawa, Y., Miyazaki, K., & Takahashi, M. (2009). On the origins of mesospheric gravity waves. Geophys. Res. Lett., 36, L19801, https://doi.org/10.1029/2009GL039908.

Sato, K., Tanteno, S., Watanabe, S., & Kawatani, Y. (2012). Gravity wave characteristics in the southern hemisphere revealed by a high-resolution middle-atmosphere general circulation model. *Journal of the Atmospheric Sciences*, 69, 1378–1396. https://doi.org/10.1175/JAS-D-11-0101.1.

Stober, G., Kuchar, A., Pokhotelov, D., Liu, H., Liu, H. L., Schmidt, H., ... & Mitchell, N. (2021). Interhemispheric differences of mesosphere–lower thermosphere winds and tides investigated from three whole-atmosphere models and meteor radar observations. *Atmospheric chemistry and physics*, 21(18), 13855-13902. doi: 10.5194/acp-21-13855-2021.

Thurairajah, B., Cullens, C. Y., Siskind, D. E., Hervig, M. E., & Bailey, S. M. (2020). The role of vertically and obliquely propagating gravity waves in influencing the polar summer mesosphere. Journal of Geophysical Research: Atmospheres, 125, e2020JD032495. https://doi.org/10.1029/2020JD032495.

Vincent, R.A. (2015). The dynamics of the mesosphere and lower thermosphere: a brief review. *Prog. in Earth and Planet. Sci.* 2, 4. https://doi.org/10.1186/s40645-015-0035-8

Vadas, S. L., Zhao, J., Chu, X., & Becker, E. (2018). The excitation of secondary gravity waves from local body forces: Theory and observation. *Journal of Geophysical Research: Atmospheres*, 123(17), 9296-9325. https://doi.org/10.1029/2017JD027970.

Xue, X. H., Liu, H. L., & Dou, X. K. (2012). Parameterization of the inertial gravity waves and generation of the quasi-biennial oscillation. *Journal of Geophysical Research: Atmospheres*, 117(D6), doi:10.1029/2011JD01.

Yiğit, E., Aylward, A. D., and Medvedev, A. S. (2008). Parameterization of the effects of vertically propagating gravity waves for thermosphere general circulation models: Sensitivity study. Journal of Geophysical Research: Atmospheres, 113(D19). DOI: https://doi.org/10.1029/2008JD010135.

Yiğit, E., A. S. Medvedev, A. D. Aylward, P. Hartogh, and M. J. Harris. (2009). Modeling the effects of gravity wave momentum deposition on the general circulation above the turbopause, J. Geophys. Res., 114, D07101. doi:10.1029/2008JD011132.

Yiğit E, Medvedev A. S., and Ern, M. (2021). Effects of Latitude-Dependent Gravity Wave Source Variations on the Middle and Upper Atmosphere. Front. Astron. Space Sci. 7:614018. doi: 10.3389/fspas.2020.614018

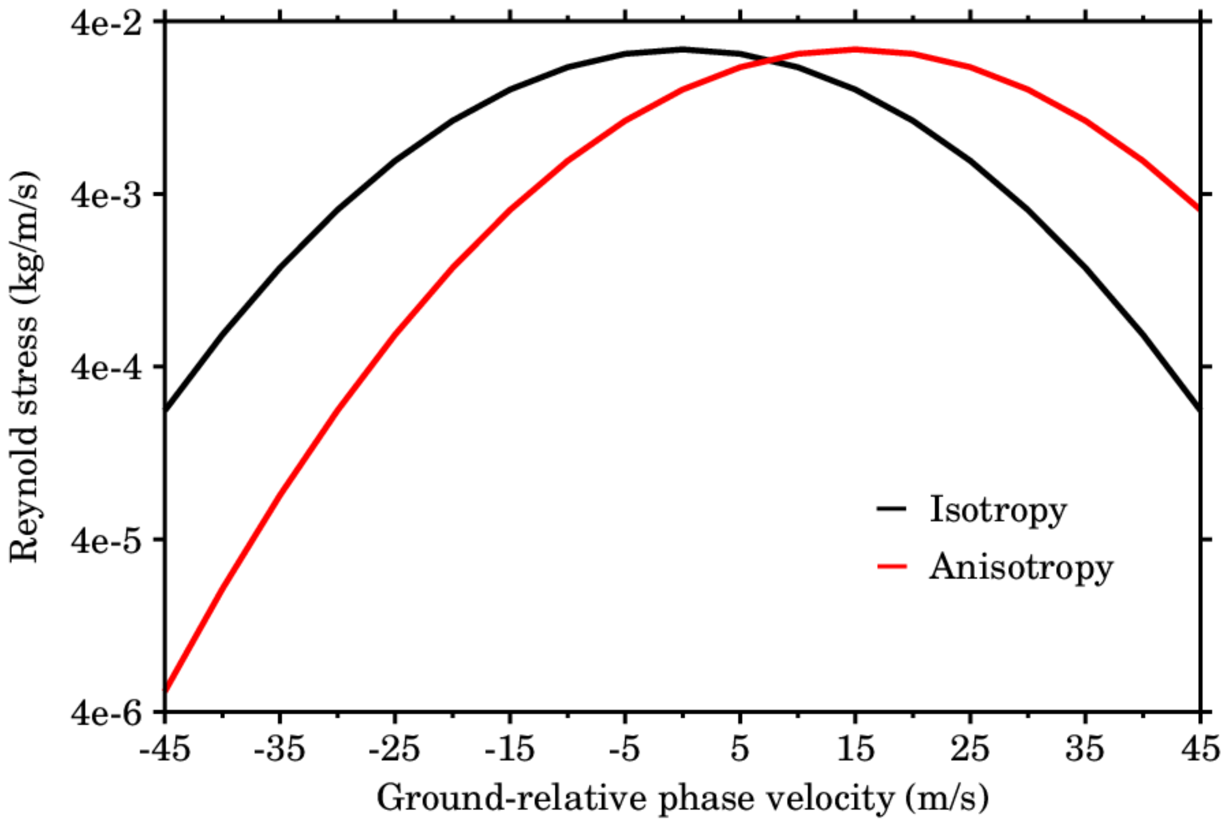

Figure 1. The concept map of the gravity wave source spectrum as a function of ground-relative phase velocity. The black and red curves denote isotropic and anisotropic spectra of gravity wave sources, respectively.

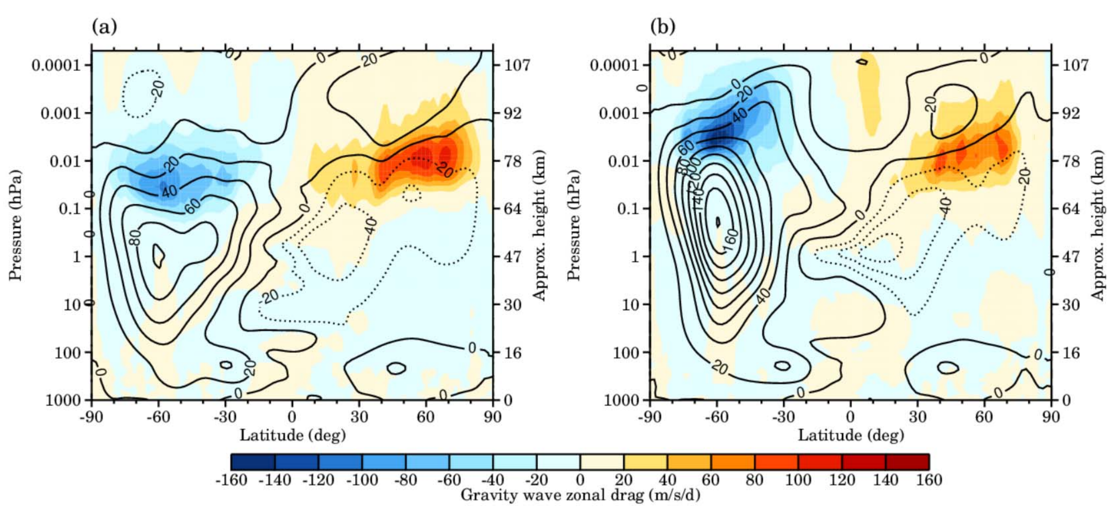

Figure 2. (a) Zonal mean zonal gravity wave drags (color shading) and zonal winds (line contours, contour interval is 20 m/s, solid and dashed lines indicate positive and negative values, respectively) in June simulated in the first year of the base case. (b) The same as (a), but for the control case 1.

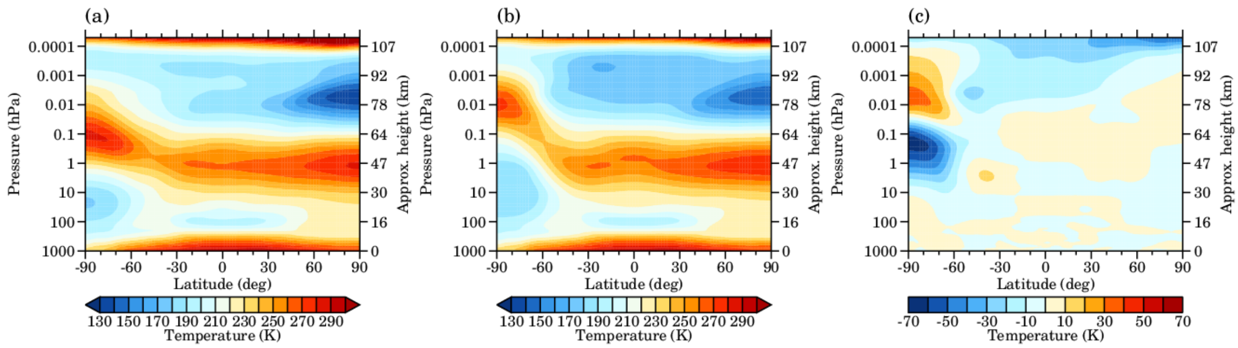

Figure 3. (a) Zonal mean temperature in June simulated in the first year of the base case. (b) The same as (a), but for the control case 1. (c) The difference between (b) and (a).

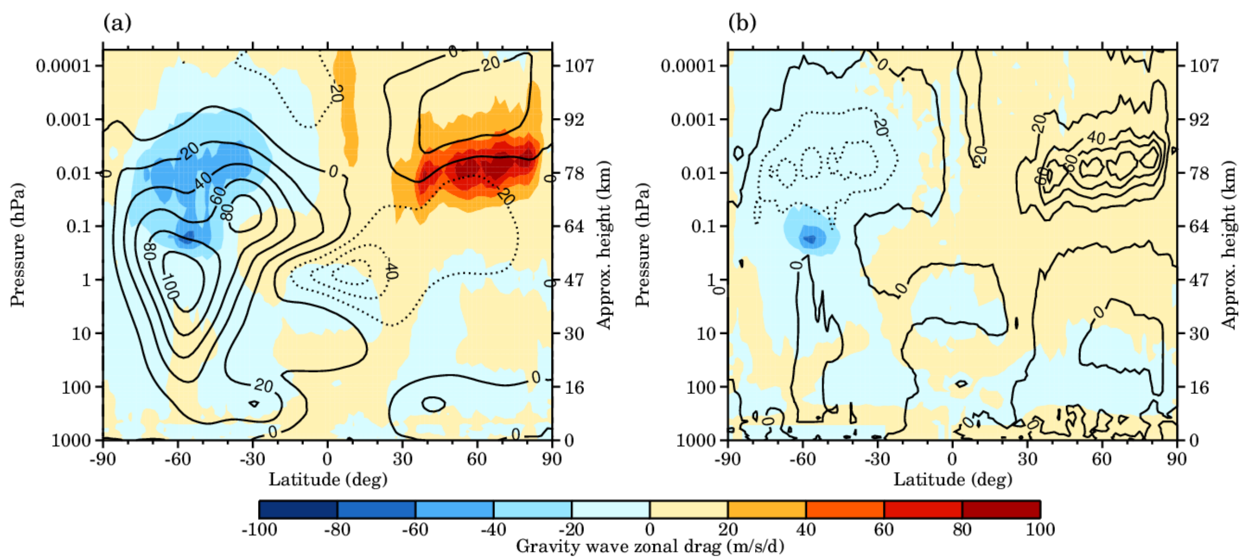

Figure 4. (a) Zonal mean zonal gravity wave drags (color shading) and zonal winds (line contours, contour interval is 20 m/s, solid and dashed lines indicate positive and negative values, respectively) in June simulated in the first year of the control case 2. (b) Zonal mean zonal

inertial gravity wave drags (color shading) and all other gravity wave drags (contours, contour interval is 20 m/s/d, solid and dashed lines indicate positive and negative values, respectively) in June simulated in the first year of the control case 2.

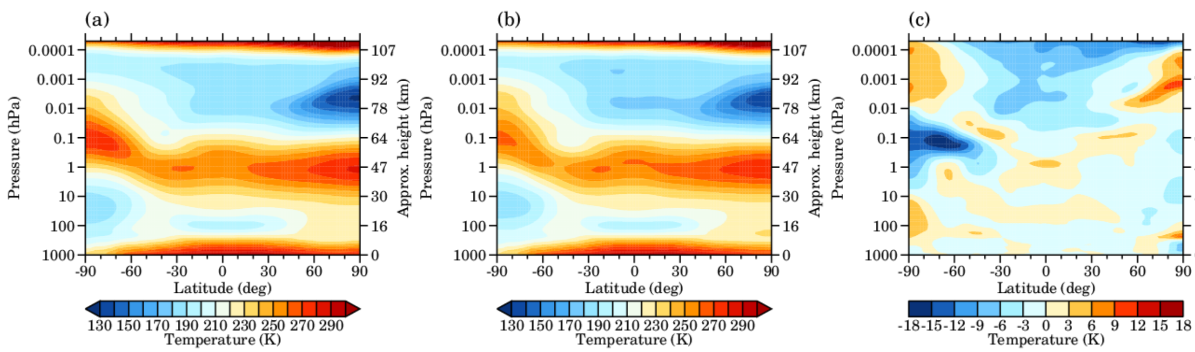

Figure 5. (a) Zonal mean temperature in June simulated in first year of the base case. (b) The same as (a), but for the first year of the control case 2. (c) The difference between (b) and (a).

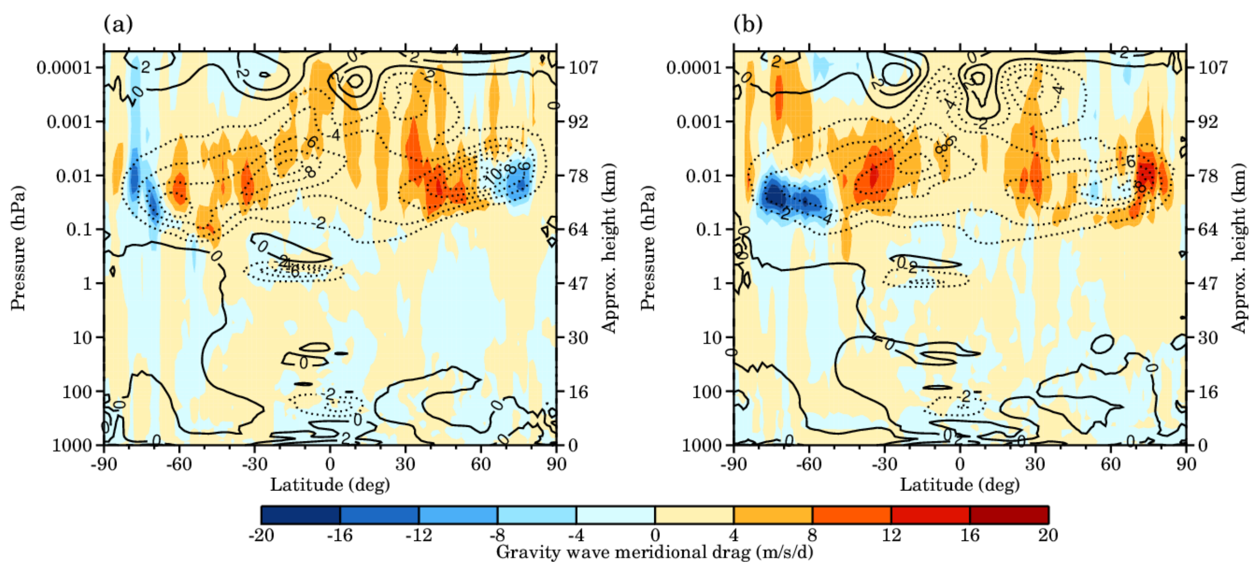

Figure 6. (a) Zonal mean meridional gravity wave drags (color shading) and meridional winds (line contours, contour interval is 2 m/s, solid and dashed lines indicate positive and negative values, respectively) in June simulated in first year of the base case. (b) The same as (a), but for the first year of the control case 2.

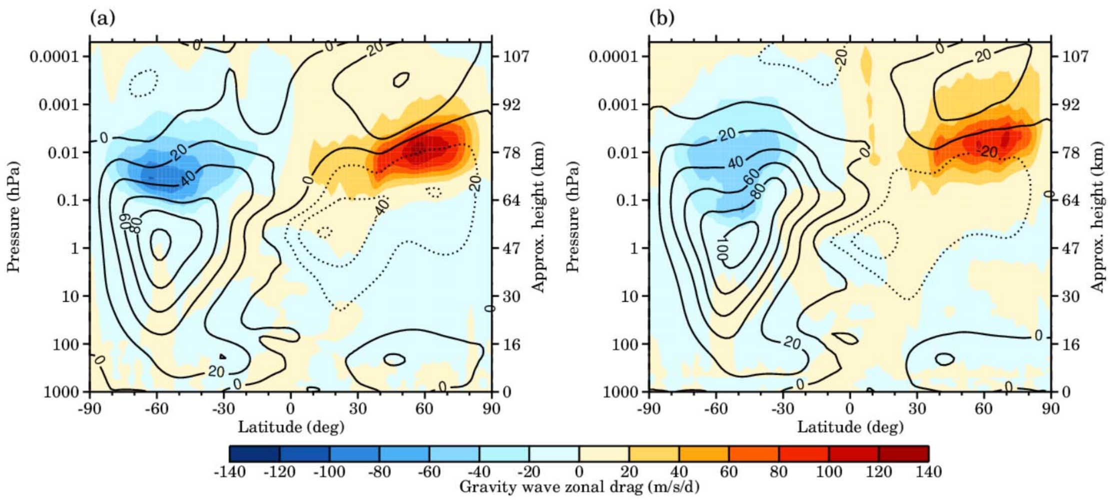

Figure 7. (a) 3-year averaged zonal mean zonal gravity wave drags (color shading) and zonal winds (line contours, contour interval is 20 m/s, solid and dashed lines indicate positive and negative values, respectively) in June simulated in the base case. (b) The same as (a), but for the control case 2.

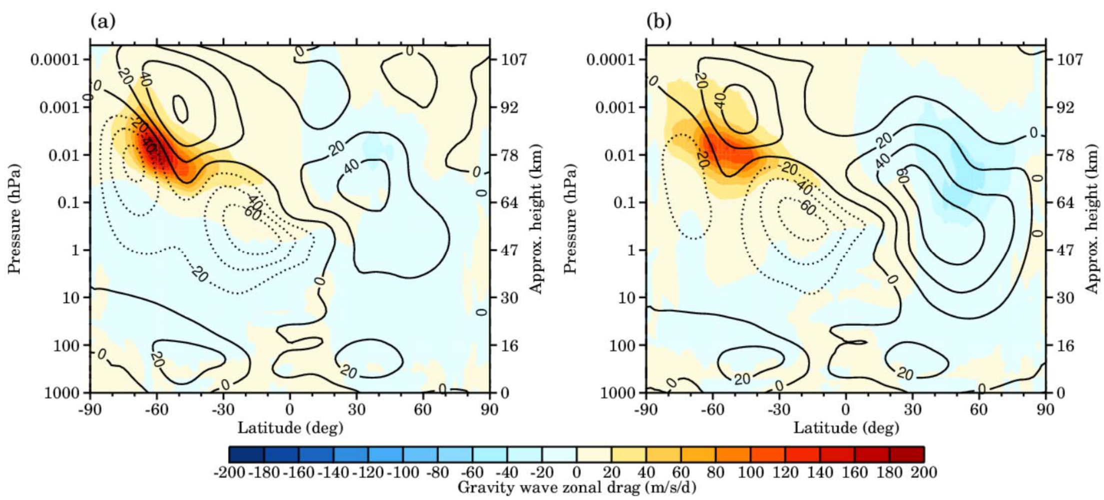

Figure 8. The same as figure 7, but in December.

Figure 1.

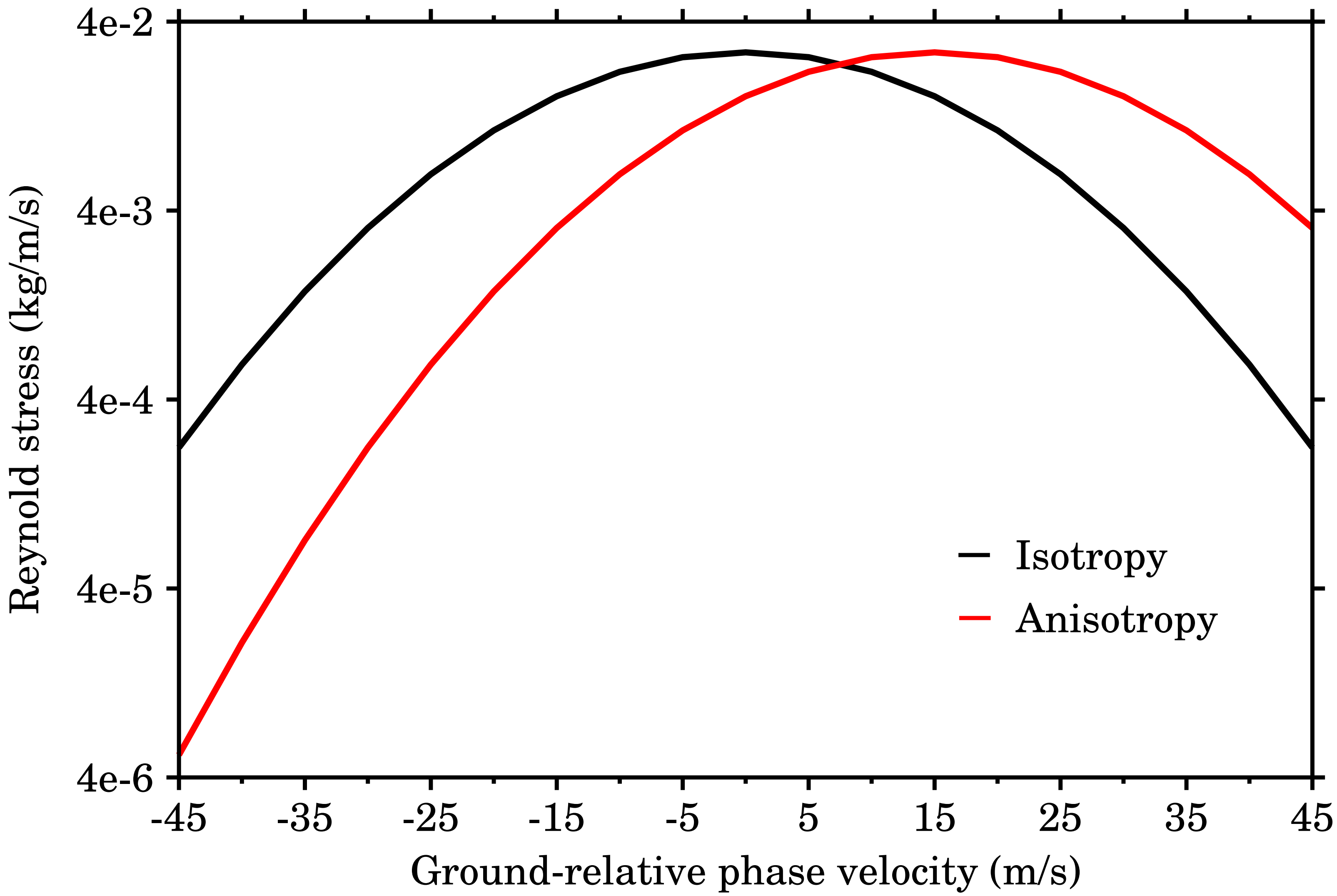

4e-2
4e-3
4e-4
4e-5
4e-6
Reynold stress (kg/m/s)
-45
-35
-25
-15
-5
5
15
25
35
45
Ground-relative phase velocity (m/s)
Isotropy
Anisotropy

Figure 2.

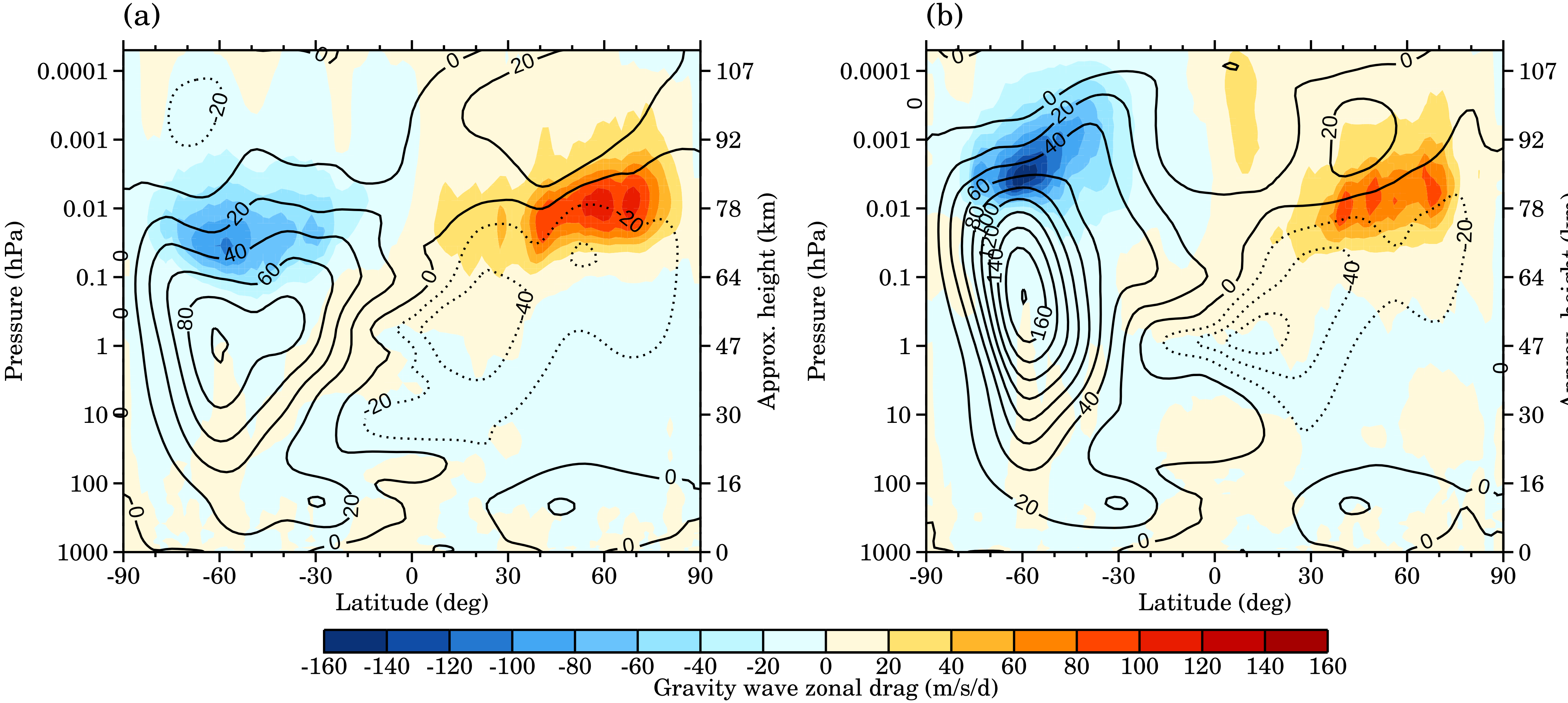

(a)
(b)
Pressure (hPa)
Approx. height (km)
Latitude (deg)
0.0001
0.001
0.01
0.1
1
10
100
1000
107
92
78
64
47
30
16
0
-90
-60
-30
0
30
60
90
-160
-140
-120
-100
-80
-60
-40
-20
0
20
40
60
80
100
120
140
160
Gravity wave zonal drag (m/s/d)

Figure 3.

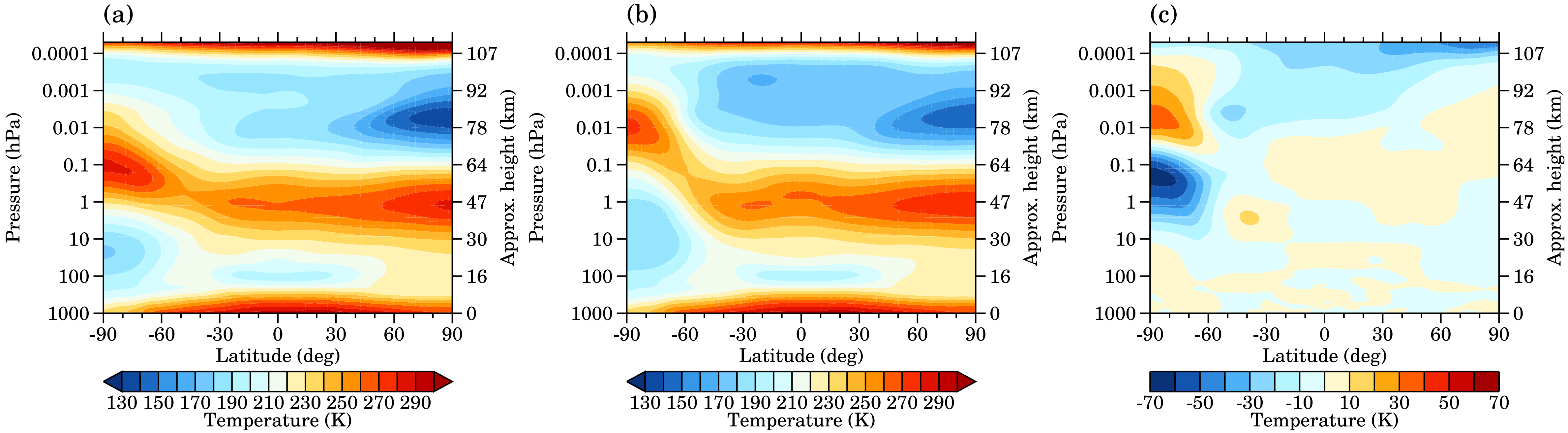
(a)
(b)
(c)
Pressure (hPa)
0.0001
0.001
0.01
0.1
1
10
100
1000
Approx. height (km)
107
92
78
64
47
30
16
0
-90
-60
-30
0
30
60
90
Latitude (deg)
130 150 170 190 210 230 250 270 290
Temperature (K)
-70 -50 -30 -10 10 30 50 70
Temperature (K)

Figure 4.

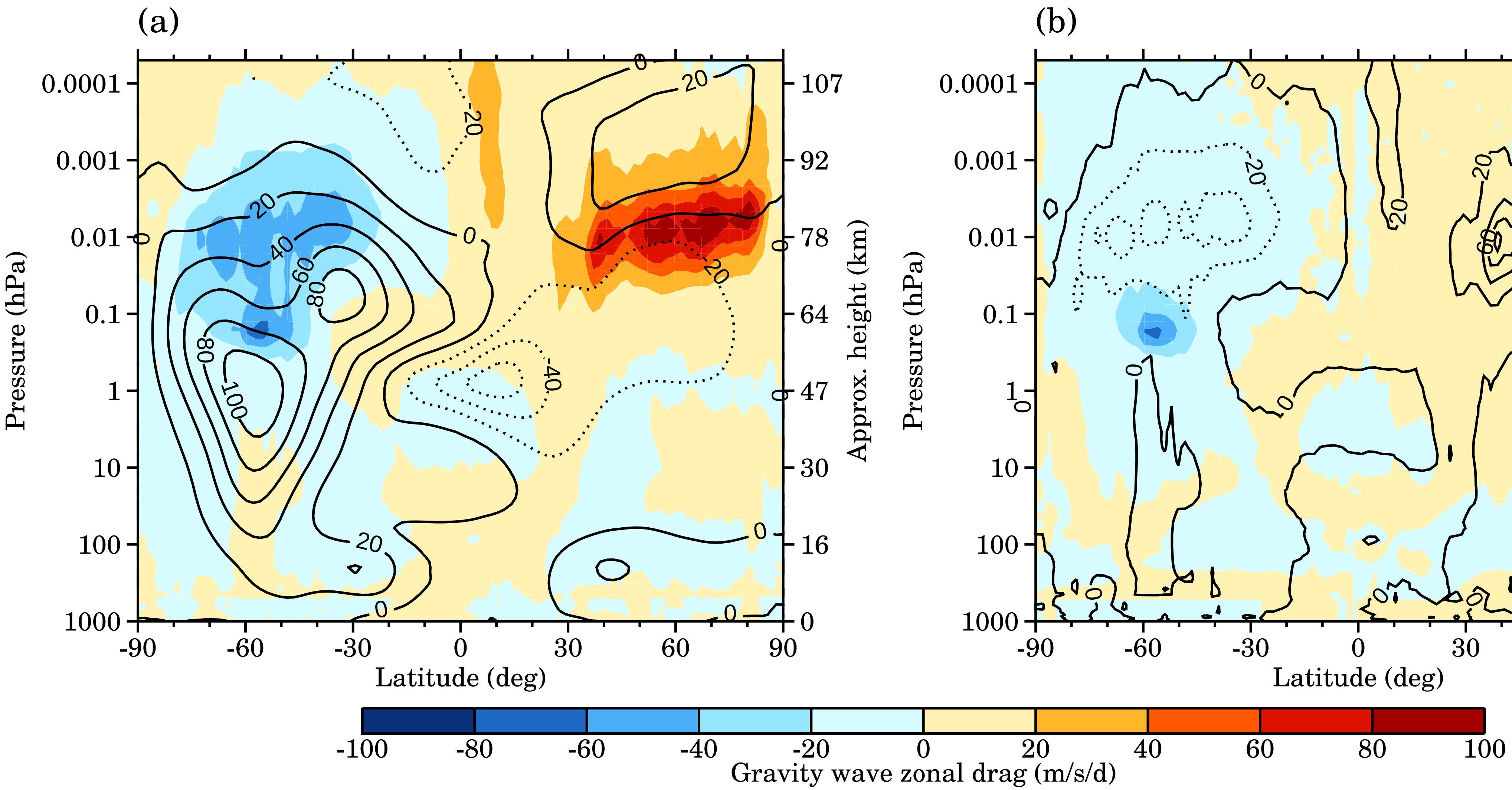
(a)
(b)
Pressure (hPa)
Approx. height (km)
Latitude (deg)
Gravity wave zonal drag (m/s/d)

Figure 5.

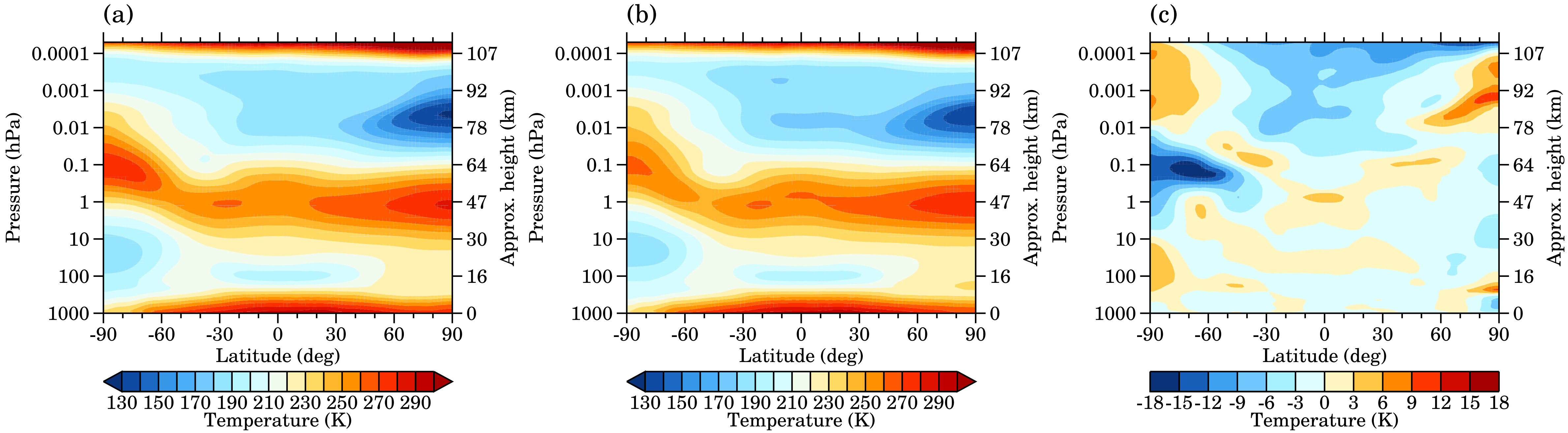
(a)
(b)
(c)
Pressure (hPa)
Approx. height (km)
Latitude (deg)
Temperature (K)
0.0001
0.001
0.01
0.1
1
10
100
1000
107
92
78
64
47
30
16
0
-90 -60 -30 0 30 60 90
130 150 170 190 210 230 250 270 290
-18 -15 -12 -9 -6 -3 0 3 6 9 12 15 18

Figure 6.

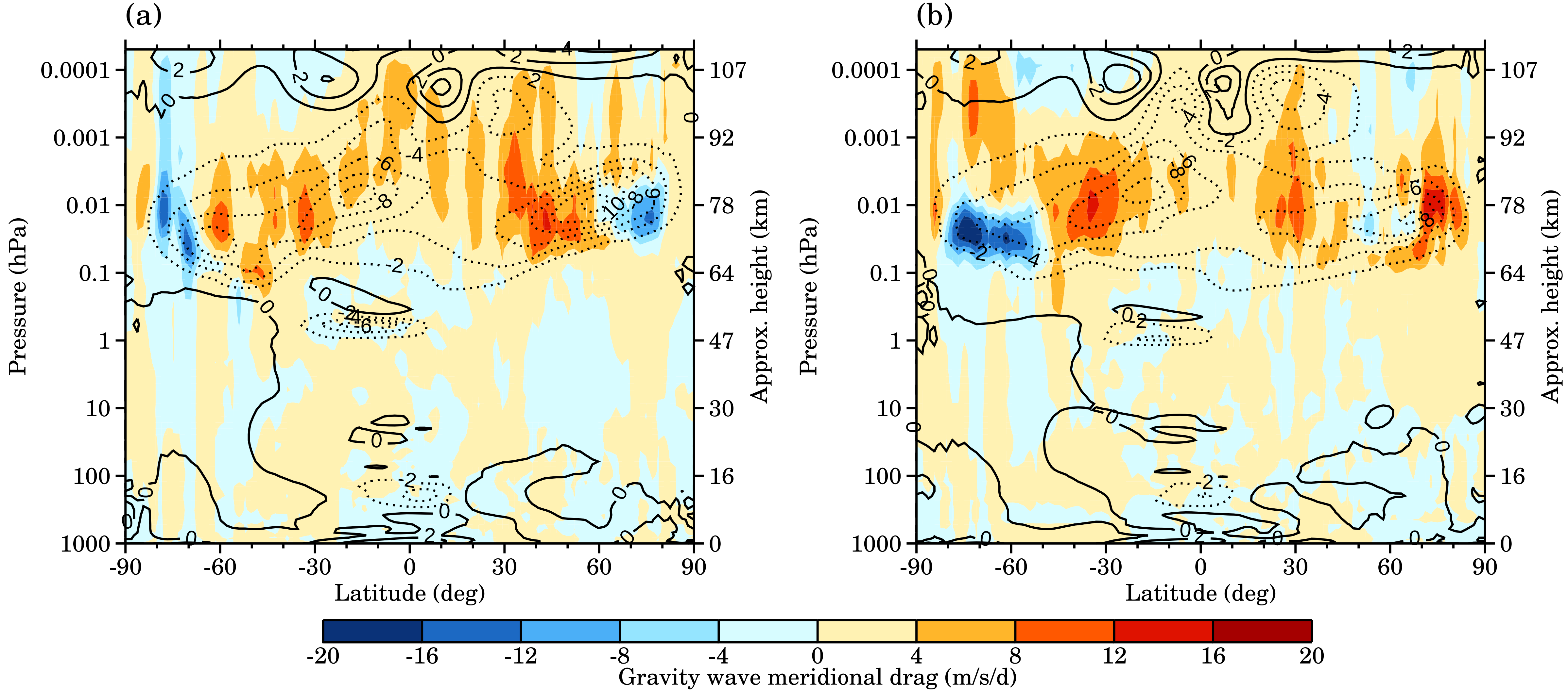

(a)
(b)
Pressure (hPa)
Approx. height (km)
Latitude (deg)
Gravity wave meridional drag (m/s/d)

Figure 7.

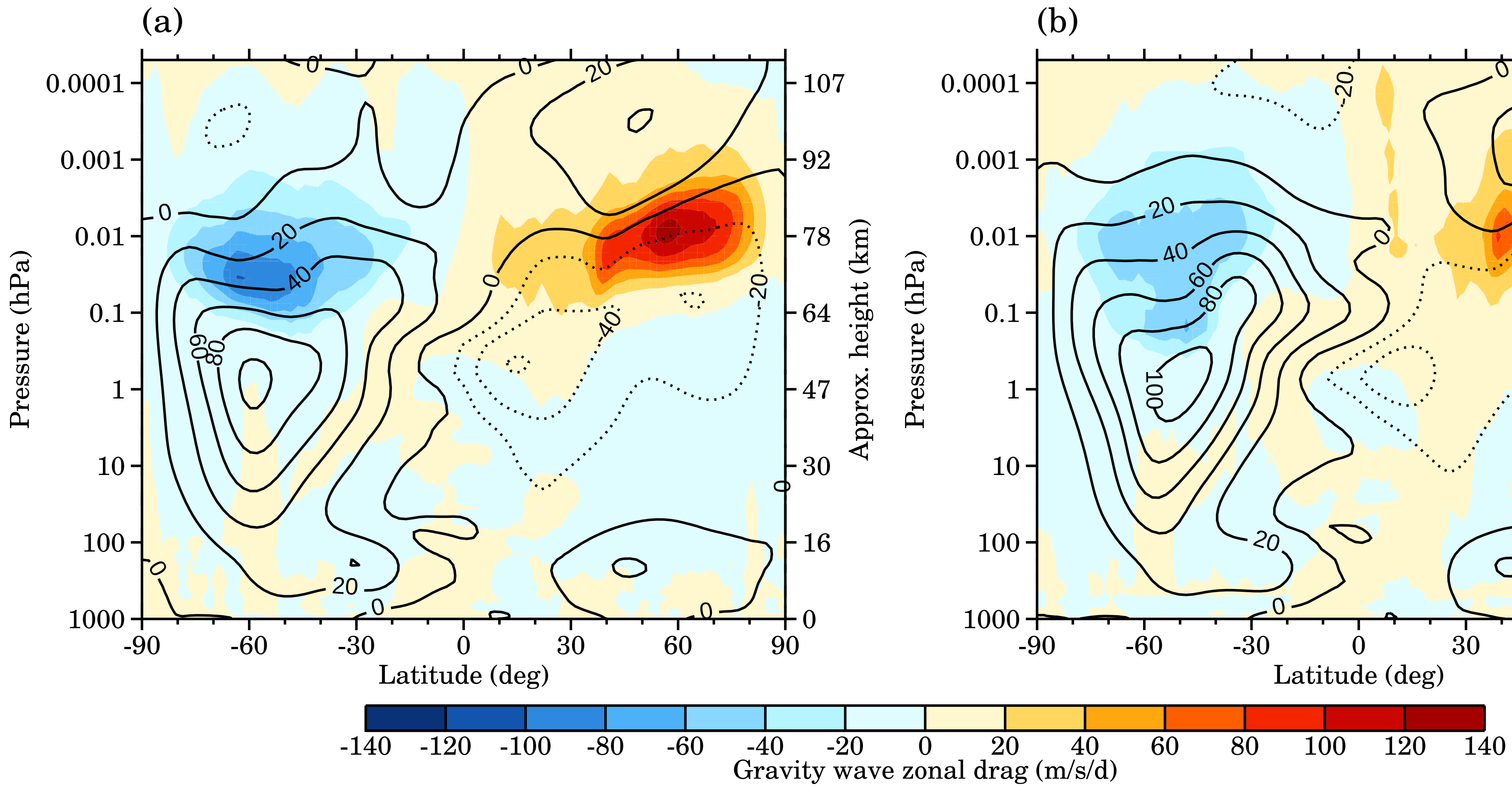

(a)
(b)
Pressure (hPa)
Approx. height (km)
Latitude (deg)
Gravity wave zonal drag (m/s/d)

Figure 8.

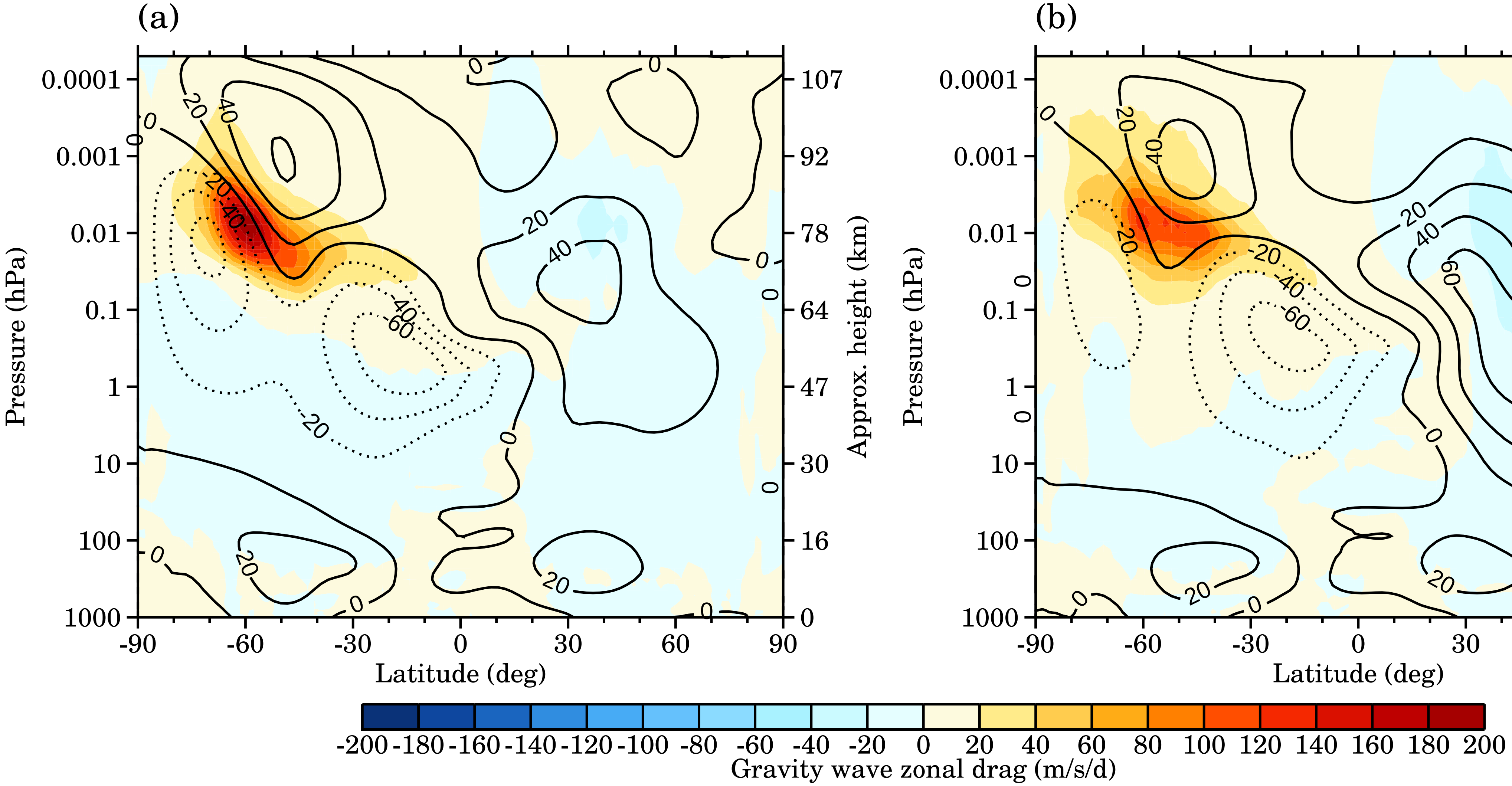
(a)
(b)
Pressure (hPa)
Approx. height (km)
Latitude (deg)
Gravity wave zonal drag (m/s/d)
-200 -180 -160 -140 -120 -100 -80 -60 -40 -20 0 20 40 60 80 100 120 140 160 180 200